PHYSICAL REVIEW APPLIED **14,** 054039 (2020)

Lateral Gate and Magnetic Field Controlled Quantum Transport in a Topological Dirac Semimetal Nanowire

Shunxi Tang,[1] Li Zhou,[1] Zhengfang Liu,[2] Qingping Wu,[2] Yangming He,[1] Jiajia Luo,[3] and Xianbo Xiao[1,*]

[1] *School of Computer Science, Jiangxi University of Traditional Chinese Medicine, Nanchang 330004, China*
[2] *School of Basic Science, East China Jiaotong University, Nanchang 330013, China*
[3] *Libaray, Jiangxi University of Traditional Chinese Medicine, Nanchang 330004, China*

(Received 28 July 2020; revised 20 September 2020; accepted 22 October 2020; published 17 November 2020)

Both the charge- and spin-transport properties of a topological Dirac semimetal (TDSM) nanowire with two lateral gates and a perpendicular magnetic field are investigated by using the Green function method in combination with the Landauer-Büttiker formula. A fully spin-polarized surface current can be generated in the considered system and it can be turned on or off by varying the electron energy and magnetic field strength. The underlying physics of this transport phenomenon originates from the quantum anomalous Hall-like insulator state of the TDSM nanowire caused by the magnetic field. Further studies indicate the spin-polarized current with a strong robustness against disorder, displaying the feasibility of designing a topological spin filtering and switch device based on the considered system.

DOI: 10.1103/PhysRevApplied.14.054039

I. INTRODUCTION

Three-dimensional (3D) topological Dirac semimetals (TDSMs) have aroused researchers' intense interest [1] since the pioneering work on the theoretical predictions of topological Dirac electron states in β-cristobalite BiO_2 [2], A_3Bi (A = Na, K, Rb) [3] and Cd_3As_2 [4]. Differing from topological insulators, this sort of topological material has no bulk gaps but crystal-symmetry-protected bulk Dirac points and gapless energy dispersion linearly along all three directions [5–9]. As a result, ultrahigh electron mobility is observed in various TDSMs [10–12], indicating their potential applications in the designment of electronic or spintronics devices with high performance. Moreover, unique Fermi-arc surface states emerge on the surfaces once the TDSMs are confined [13–15]. On the other hand, TDSMs are excellent platforms to study topological phase transitions, i.e., they may be transited into other phases including band insulator [16,17], topological insulator [18,19], topological Anderson insulator [20], Weyl semimetal [21–24], topological superconductor [25], etc. by breaking certain symmetries.

Understanding the quantum-transport properties of TDSMs is not only one of the key prerequisites in designing topological electronic or spintronics devices but also an efficient method to apprehend their electronic characteristics. Linear positive magnetoresistance is observed in TDSMs when a perpendicular magnetic field (MF) with respect to the transport direction is applied [26–28]. However, giant negative magnetoresistance is achieved as a parallel MF is added [29–34], revealing the chiral anomaly of electrons in the TDSMs. Anisotropic electron transmission behaviors found in the junctions consist of TDSM films without and with a MF at various in-plane directions [35]. Spin-filter effect is generated in the hybrid TDSM and circularly-polarized-light-irradiated Weyl semimetal and TDSM structures due to the emergence of a new Weyl half-metal phase [36]. Further, abrupt changes happen in the high-field magnetoresistance of TDSM $ZrTe_5$, indicating mass generation of the interacting Dirac fermions [37]. Recently, another transport phenomenon, namely three-dimensional quantum Hall effect is observed in Cd_3As_2 [38] and $ZrTe_5$ [39], which are attributed to the Weyl orbits [40] and charge density waves formed in the two systems, respectively.

However, up to now, electronic structures and quantum-transport properties of TDSM nanostructures have been paid less attention. Owing to the confining effect, large surface-to-volume ratio of TDSM nanostructures reduces the bulk carrier density so that surface states dominate the transport behaviors. Therefore, Fano-resonance-like asymmetric structure appears in the differential conductance spectrum of TDSM nanowires, resulting from the interference between the confinement-induced discrete surface states and continuous bulk states [41]. The spin-momentum locking property of the surface states in TDSM nanowires is confirmed by the spin-transport-measurement experiments [42]. In addition, in our recent

---

[*] 20101034@jxutcm.edu.cn

© 2020 American Physical Society

work, anisotropic finite-size effect [43] and magnetoelectronic structures and magnetotransport [44] are found in TDSM nanostructures.

In this paper, we investigate the quantum transport in a TDSM nanowire in the presence of two lateral gates and a perpendicular MF by adopting the tight-binding Green function (GF) method combined with the Landauer-Büttiker (LB) formula. It is found that the positions of the surface energy levels corresponding to the Fermi arc of the TDSM nanowire can be shifted by varying the lateral gate voltage. Moreover, the Zeeman-like spin-splitting phenomenon is observed in both bulk and surface energy levels even when the Zeeman effect of the MF is not included. Therefore, both the charge and spin transport in the TDSM nanowire can be switched on or off by tuning the electron energy and MF magnitude, demonstrating that a topological spin filtering and switch device based on the considered system can be constructed. The physical mechanism of the interesting transport phenomena of the TDSM nanowire is analyzed by analytic calculations. Further studies show that the surface-state transport is robust against disorders, which means the proposed topological spin filtering and switch device with the potential for practical applications.

The rest of this paper is arranged as follows. In Sec. II, a theoretical model of the considered system and calculation methods are presented. In Sec. III, numerical results, analytic analyses, and discussions are demonstrated. Finally, Sec. IV concludes the paper.

II. MODEL AND METHODS

The investigated system is schematically illustrated in Fig. 1, where a TDSM nanowire confined along both the y and z axis is connected semi-infinite electron source and drain electrodes along the x axis at each end. The transversal widths of the nanowire are W_y and W_z, and its length is L_x. Two lateral gates along the y axis are attached to the TDSM nanowire, and two insulator layers are inserted between the nanowire and lateral gates to avoid transversal current. On the other hand, a perpendicular MF along the z axis is applied to the TDSM nanowire.

Based on the four orbital bases $|s_{1/2}, \frac{1}{2}\rangle$, $|p_{3/2}, \frac{3}{2}\rangle$, $|s_{1/2}, -\frac{1}{2}\rangle$, and $|p_{3/2}, -\frac{3}{2}\rangle$ near the Fermi level, the low-energy effective electron Hamiltonian around the Γ point in the first Brillouin zone of TDSM A_3Bi (A = Na, K, Rb) [3] and Cd_3As_2 [4] reads

$$H(\mathbf{k}) = \epsilon_0(\mathbf{k}) + \begin{bmatrix} M(\mathbf{k}) & Ak_+ & 0 & 0 \\ Ak_- & -M(\mathbf{k}) & 0 & 0 \\ 0 & 0 & M(\mathbf{k}) & -Ak_- \\ 0 & 0 & -Ak_+ & -M(\mathbf{k}) \end{bmatrix}, \tag{1}$$

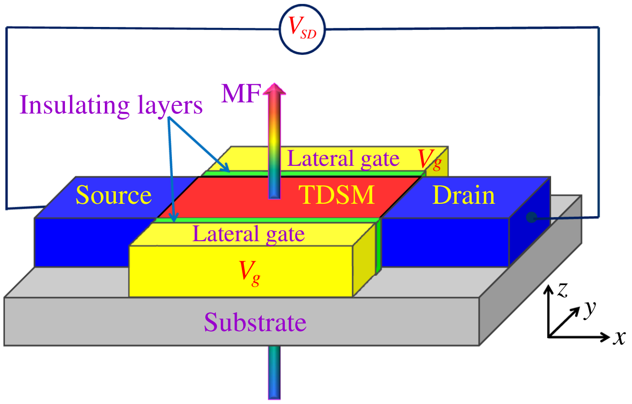

FIG. 1. Schematic figure showing the TDSM-nanowire-based device. It consists of two metal electrodes and a TDSM nanowire with two lateral gates and a perpendicular MF. Two insulating layers are inserted between the nanowire and lateral gates to avoid transversal electric current.

in which $\epsilon_0(\mathbf{k}) = C_0 + C_1k_z^2 + C_2(k_x^2 + k_y^2)$, $k_\pm = k_x \pm ik_y$, and $M(\mathbf{k}) = M_0 - M_1k_z^2 - M_2(k_x^2 + k_y^2)$. The parameters A, C_i, and M_i $(i = 0,\ 1,\ 2)$ in this Hamiltonian can be obtained by fitting the *ab initio* calculation results for a concrete TDSM material. According to the nearest tight-binding approximation, the TDSM nanowire in Fig. 1 can be modeled by discretizing Eq. (1) onto a 3D cubic lattice with the lattice constants a_x, a_y, and a_z [43]. The effect of the lateral gates is adopted by adding a static electric potential eV_g to the on-site energy of the lattices, where ($-e$) is the electron charge and V_g the gate voltage. However, due to the shielding effect of the lateral gates, only the lattices situated within the Debye (shielding) length in the TDSM nanowire are subjected to the static electric potential. The Debye length is given by $L_D = \sqrt{\varepsilon_r\varepsilon_0k_BT/e^2n}$, in which ε_r and ε_0 are the relative dielectric constant and the permittivity of vacuum, respectively. k_B is Boltzmann constant, T is temperature, and n denotes the electron density in the TDSM nanowire. In addition, the influence of the perpendicular MF $\mathbf{B} = (0, 0, B_z)$ is studied by introducing the Peierls phase factor $e^{i(2\pi/\phi_0)\int_{\mathbf{R}_i}^{\mathbf{R}_j}\mathbf{A}\cdot d\mathbf{R}}$ to the hopping energy between the nearest lattices with position vectors $\mathbf{R}_i$ and $\mathbf{R}_j$, where the magnetic vector potential is taken as $\mathbf{A} = (B_zy, 0, 0)$ and $\phi_0 = h/2e$ is the magnetic flux quanta with the Planck constant h [44]. It should be noted that the Zeeman effect of the MF is not considered first, since it does not alter the intrinsic conclusions.

For the quantum transport in the considered system, it can be calculated by using the recursive GF method based on the discretized Hamiltonian of Eq. (1) [43]. The detail calculation procedure of the retarded and advanced GF of the considered system G^r and G^a [$G^a = (G^r)^\dagger$] can be found in the previous works [45,46] so that they are not presented here for conciseness. Taking the effects of the semi-infinite source and drain electrodes into account, the spin-dependent conductance of the whole system is given by the LB formula [47,48]

$$G^{\sigma\sigma'} = \frac{e^2}{h}\sum_{i,j=1}^{N} |t_{ij}^{\sigma\sigma'}|^2, \tag{2}$$

in which $t_{ij}^{\sigma\sigma'}$ is the spin-dependent transmission coefficient of electrons in the source electrode injected from the mode i with spin σ to the output mode j with spin σ' in the drain electrode. N is the number of the propagating modes. As there is no spin-precession mechanism in the considered system, the two-terminal charge and spin conductances are defined in terms of the spin-dependent conductance in Eq. (2) as [49]

$$G^C = G^{\uparrow\uparrow} + G^{\downarrow\downarrow}, \tag{3}$$

and

$$G^S = \frac{e}{4\pi}\frac{G^{\uparrow\uparrow} - G^{\downarrow\downarrow}}{e^2/h}, \tag{4}$$

respectively. ↑(↓) denotes the spin-up (-down) state of electrons.

III. NUMERICAL RESULTS, ANALYTICAL ANALYSES, AND DISCUSSIONS

In the following numerical and analytic calculations, the concrete material parameters of the TDSM nanowire are taken as those for the $\mathrm{Na_3Bi}$, which are obtained from the *ab initio* calculations [3]. $C_0 = -63.82$ meV, $C_1 = 87.536$ meV nm^2, $C_2 = -84.008$ meV nm^2, $M_0 = -86.86$ meV, $M_1 = -106.424$ meV nm^2, $M_2 = -103.610$ meV nm^2, and $A = 245.98$ meV nm. The lattice constants are set at $a_x = a_y = 0.6$ nm and $a_z = 0.5$ nm. The geometrical structure parameters of the nanowire are chosen to $W_y = 15\ a_y$ and $W_z = 10a_z$, and $L_x = 50a_x$. The δ-function potential approximation for the effect of the lateral gates is adopted, i.e., only the outmost lattices along the y axis are subjected to the static electric potential. This approximation can be guaranteed by tuning the Debye length in the TDSM nanowire since it depends on the electron density ($n \sim 10^{18}$ cm^{-3}) and temperature of the $\mathrm{Na_3Bi}$ nanowrie [50]. For the source and drain electrodes, in general, can be any metals. The essential results and underlying physics that we discuss below are independent of the specific material. However, in order to decrease as much as possible the contact resistance, the material of the source and drain electrodes is used as the same as that of the TDSM nanowire. In addition, the magnetic flux through a unit square $\phi = B_z a_x a_y$ is in units of the magnetic flux quanta ϕ_0. The charge and spin conductances are in units of e^2/h and $e/(4\pi)$, respectively.

Energy band of the pristine infinite TDSM nanowire is shown in Fig. 2(a). Due to the quantum-confining effect, the continuous gapless linear bulk energy band is lifted into parabolic subbands and bulk gap is opened, as shown by the dark-cyan solid lines. The bulk gap depends on both the nanowire widths W_y and W_z. The magnitude of the bulk gap decreases monotonously with the increasing width W_y (approximately W_y^{-1}), as shown by the violet solid line in the inset. However, it displays a periodic oscillating behavior with the increase of the width W_z [43]. At the same time, the wavevector along the z axis is quantized into $k_{zm} = m\pi/W_z = 0.628m$ (nm^{-1}), where m is the subband index. In this case, the wavevector of the first subband $k_{z1} = 0.628$ (nm^{-1}) is situated between the two Dirac points $k_D = \pm\sqrt{M_0/M_1} = \pm 0.903$ (nm^{-1}).

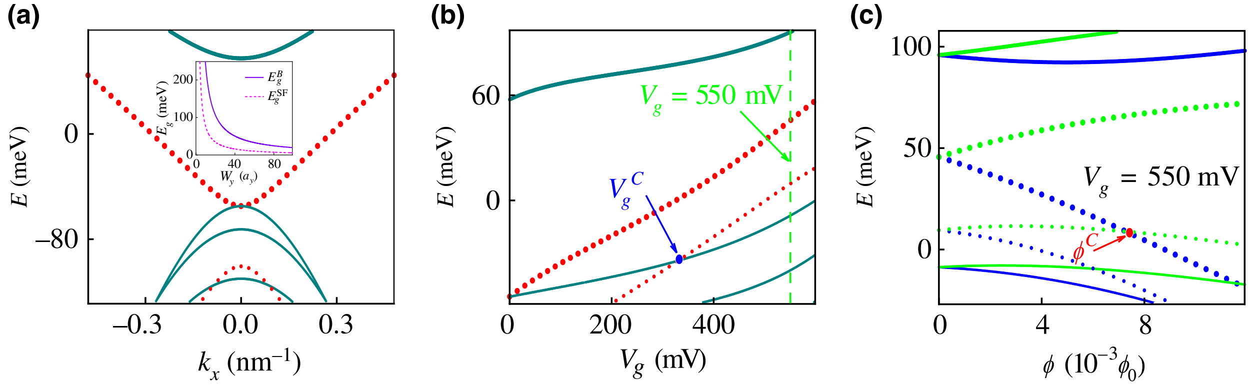

FIG. 2. (a) Energy band of an extended pristine TDSM nanowire with widths of $W_y = 15\ a_y$ and $W_z = 10\ a_z$, showing topological surface subbands (red dotted lines) and bulk subbands (dark cyan solid lines). Inset displays both the bulk (violet solid line) and surface (magenta dashed line) band gaps of the TDSM nanowire as a function of the wire width W_y. (b) Subband edge energies ($k_x = 0$) of the TDSM nanowire with two lateral gates versus the gate voltage. (c) Subband edge energies ($k_x = 0$) of the TDSM nanowire in the presence of both two lateral gates and a perpendicular MF versus the magnetic flux. The gate voltage is taken as $V_g = 550.0$ mV, as indicated by the vertical green dashed line in Fig. 2(b).

Therefore, the band gap for this subband is inverted and the TDSM nanowire is topological nontrival in this case [4,20]. Therefore, surface subbands emerge in the energy band, as shown by the red dotted lines. For clearness, only the lowest surface subband is presented here. Similar to that of topological insulators [51], the overlap of the two surface electron wave functions at the opposite lateral surfaces (along the y axis) of the TDSM nanowire induces a small gap opened in the surface band. The surface band gap of the TDSM nanowire as a function of the width W_y is shown by the red dashed line in the inset. It decreases exponentially as the width W_y is increased. However, differing from those of the topological insulators, both the surface conduction subband minimum and valence subband maximum are buried in the bulk valence subbands. As a result, the lowest surface conduction subband penetrates throughout the bulk energy gap. Therefore, it will always be conducted when the Fermi energy is located within the bulk energy gap. First, we consider the effects of the lateral gates. Subband edge energies ($k_x = 0$) of the TDSM nanowire as a function of the lateral gate voltage are plotted in Fig. 2(b). Both the bulk and surface subband edge energies move upwards with increasing gate voltage. However, the energies of the surface subband edges are increased linearly since the lateral gates mainly influence the surface lattices along the y axis. The slope of the surface subband edge energy spectra is about 0.18, agrees approximately to the ratio of the lattices with and without the static electric potential $2/(W_y/a_y - 1)$. More importantly, the surface valence maximum is shifted into the bulk band gap as the gate voltage is increased to $V_g^C = 330.0$ mV. As a result, both the surface conduction and valence edges are situated within the bulk gap when the gate voltage is increased further. Then, the effects of the perpendicular MF are taken into account as well. Subband edge energies ($k_x = 0$) of the TDSM nanowire as a function of the magnetic flux ϕ is depicted in Fig. 2(c). The lateral gate voltage is taken as $V_g = 550.0$ mV, as indicated by the vertical green dashed line in Fig. 2(b). Interestingly, each bulk and surface subband is split as the MF effect is included and the energy width between each pair of the split subbands increases with the increase of the magnetic flux ($\propto B_z$). Consequently, the lower-surface conduction subband and the upper-surface valence subband will touch together as the magnetic flux is increased to $\phi^C = 7.4 \times 10^{-3}$, demonstrating that the surface band gap is closed. As the magnetic flux is increased further, the upper-surface valence subband will surpass the lower-surface conduction subband.

In order to apprehend the characteristics of the energy band obtained in Fig. 2(c), both the two-terminal charge- and spin-conductance maps of the TDSM nanowire in the presence of the lateral gates and MF are shown in Figs. 3(a) and 3(b), respectively. As we can see, both the charge and spin conductances of the considered system can be tuned by varying the electron energy or/and the MF strength. Therefore, different quantum regions of the TDSM nanowire can be classified by the amplitudes of the charge and spin conductances. For the region with $(G^C, G^S) = (0, 0)$, which means that both the charge and spin currents are switched off. This region is corresponding to the normal-insulator (NI) state of the considered system, as shown by NI in Fig. 3(c). For the region with $(G^C, G^S) = (1, \pm 1)$, indicating that the surface current in the consider system is completely spin polarized. Therefore, these two areas represent a quantum anomalous Hall-like insulator (QAHLI) state, as shown by QAHLI in Fig. 3(c). This effect also reflects that the subbands in Fig. 2(c) are Zeeman-like spin split. The QAHLI state in the TDSM nanowire is similar to the QAH in Weyl semimetals when the chemical potential is located at the Weyl nodes [1]. However, the QAHLI state here depends on both the bulk and surface gaps induced by the finite-size effect and the Zeeman-like spin-split effect caused by the perpendicular MF. For the region with $(G^C, G^S) = (2, 0)$, which means that only the surface charge conductance is achieved while the surface spin conductance is turned off. Consequently, these three areas represent the QSHLI state, as shown by

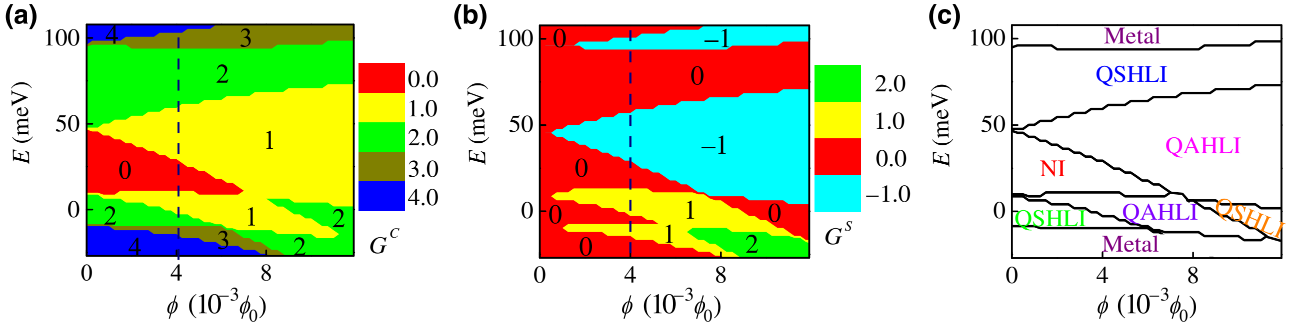

FIG. 3. (a) Charge- and (b) spin-conductance maps of the TDSM nanowire with two lateral gates and a perpendicular MF versus the electron energy and magnetic flux. (c) The quantum-state diagram of the TDSM nanowire. The gate voltage is chosen to be the same as that in Fig. 2(c).

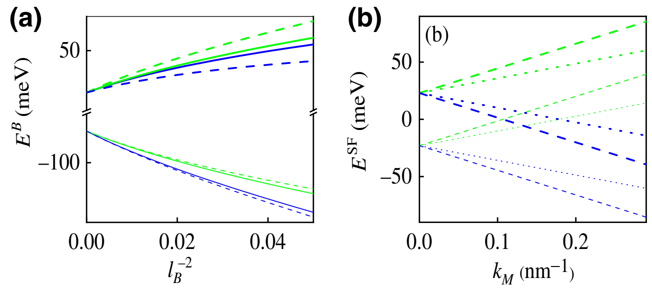

FIG. 4. (a) The lowest bulk LLs of the TDSM nanofilm without (the solid lines) and with (the dashed lines) Zeeman effect versus the negative quadratic magnetic wave vector. (b) The lowest-surface subband-edge energies ($k_x = 0$) of the TDSM nanowire without (the dotted lines) and with (the dashed lines) Zeeman effect versus the magnetic wave vector. The blue lines stand for the spin-down subbands while the green lines for the spin-up ones.

QSHLI in Fig. 3(c). Except for the above regions, the bulk state of the TDSM nanowire is also involved in the transport so that the considered system is located at a normal metal region. Moreover, according to the analyses above, topological quantum-state transitions can be achieved in the considered system by tuning the electron energy and MF strength.

The most interesting transport phenomenon above is the QAHLI-state-induced spin-polarized current in the TDSM nanowire. The underlying physics of this effect is investigated next. For the TDSM with a perpendicular MF, the Hamiltonian of the bulk Dirac electron is taken the form as

$$H^B(\mathbf{k}) = \epsilon^B(\mathbf{k}) + \begin{bmatrix} M^B(\mathbf{k}) & Ak_+^B & 0 & 0 \\ Ak_-^B & -M^B(\mathbf{k}) & 0 & 0 \\ 0 & 0 & M^B(\mathbf{k}) & -Ak_-^B \\ 0 & 0 & -Ak_+^B & -M^B(\mathbf{k}) \end{bmatrix}, \tag{5}$$

where $\epsilon^B(\mathbf{k}) = C_0 + C_1 k_z^2 + C_2[(k_x - eB_z y/\hbar)^2 + k_y^2]$, $M^B(\mathbf{k}) = M_0 - M_1 k_z^2 - M_2[(k_x - eB_z y/\hbar)^2 + k_y^2]$, and $k_\pm^B = [(k_x - eB_z y/\hbar) \pm ik_y]$. For the sake of diagonalizing this Hamiltonian, Landau-level (LL) ladder operators are defined in the standard means as

$$\begin{aligned} a^\dagger &= -\frac{l_B}{\sqrt{2}}\left[\left(k_x + \frac{y}{l_B^2}\right) + ik_y\right], \\ a &= -\frac{l_B}{\sqrt{2}}\left[\left(k_x - \frac{y}{l_B^2}\right) - ik_y\right], \end{aligned} \tag{6}$$

in which $l_B = \sqrt{\hbar/eB_z}$ is the magnetic length. And these two ladder operators obey the canonical commutation relation $[a, a^\dagger] = 1$. As a result, the Hamiltonian in Eq. (5) can be rewritten according to the ladder operators as

$$H^B(a, a^\dagger, k_z) = \begin{bmatrix} \varepsilon_+^B & -\eta a^\dagger & 0 & 0 \\ -\eta a & \varepsilon_-^B & 0 & 0 \\ 0 & 0 & \varepsilon_+^B & \eta a \\ 0 & 0 & \eta a^\dagger & \varepsilon_-^B \end{bmatrix}, \tag{7}$$

in which $\eta = \sqrt{2}A/l_B$, $\varepsilon_\pm^B = \epsilon^B(a, a^\dagger, k_z) \pm M^B(a, a^\dagger, k_z)$. Here $\epsilon^B(a, a^\dagger, k_z) = C_0 + C_1 k_z^2 + \omega_c(a^\dagger a + \frac{1}{2})$ with $\omega_c = (2/l_B^2)C_2$, and $M^B(a, a^\dagger, k_z) = M_0 - M_1 k_z^2 - \omega_m(a^\dagger a + \frac{1}{2})$ with $\omega_m = (2/l_B^2)M_2$.

For simplicity, the TDSM nanofilm is taken for the following analytical calculations since its results are similar to those of the TDSM nanowire essentially. According to Eq. (7), the eigenstates of the TDSM nanofilm in the presence of the perpendicular MF have a general form as

$$\begin{aligned} |m, n\rangle = {} & u_{m,n,\uparrow}|m, n, \uparrow\rangle + u_{m,n,\uparrow}|m, n-1, \uparrow\rangle \\ & + u_{m,n,\downarrow}|m, n-1, \downarrow\rangle + u_{m,n,\downarrow}|m, n, \downarrow\rangle, \end{aligned} \tag{8}$$

in which m and n denote the confinement-induced subband index ($m = 1, 2, \ldots$) and LL index ($n = 0, 1, 2, \ldots$), respectively. $|m, n, \uparrow(\downarrow)\rangle$ is the mth and nth eigenvector with spin up (down). $u_{m,n,\uparrow(\downarrow)}$ is the corresponding complex four-component spinor wave function. Therefore, Eq. (7) is transformed into the following matrix:

$$H^B(m, n) = \begin{bmatrix} \varepsilon_+^B(m, n) & -\sqrt{n}\eta & 0 & 0 \\ -\sqrt{n}\eta & \varepsilon_-^B(m, n-1) & 0 & 0 \\ 0 & 0 & \varepsilon_+^B(m, n-1) & \sqrt{n}\eta \\ 0 & 0 & \sqrt{n}\eta & \varepsilon_-^B(m, n) \end{bmatrix}, \tag{9}$$

where $\varepsilon_\pm^B(m, n) = (C_0 \pm M_0) + (C_1 \mp M_1)(m\pi/W_z)^2 + (\omega_c \pm \omega_m)(n + \frac{1}{2})$. Diagonalizing the equation above, the eigenvalues of the subbands with spin up are obtained

$$\begin{aligned} E_{\pm,\uparrow}^B(m, n) = {} & C_0 + C_1\left(\frac{m\pi}{W_z}\right)^2 + n\omega_c + \omega_m/2 \\ & \pm \sqrt{n\eta^2 + \left[M_0 - M_1\left(\frac{m\pi}{W_z}\right)^2 + n\omega_m + \omega_c/2\right]^2}. \end{aligned} \tag{10}$$

Similarly, those for the spin down are

$$\begin{aligned} E_{\pm,\downarrow}^B(m, n) = {} & C_0 + C_1\left(\frac{m\pi}{W_z}\right)^2 + n\omega_c - \omega_m/2 \\ & \pm \sqrt{n\eta^2 + \left[M_0 - M_1\left(\frac{m\pi}{W_z}\right)^2 + n\omega_m - \omega_c/2\right]^2}. \end{aligned} \tag{11}$$

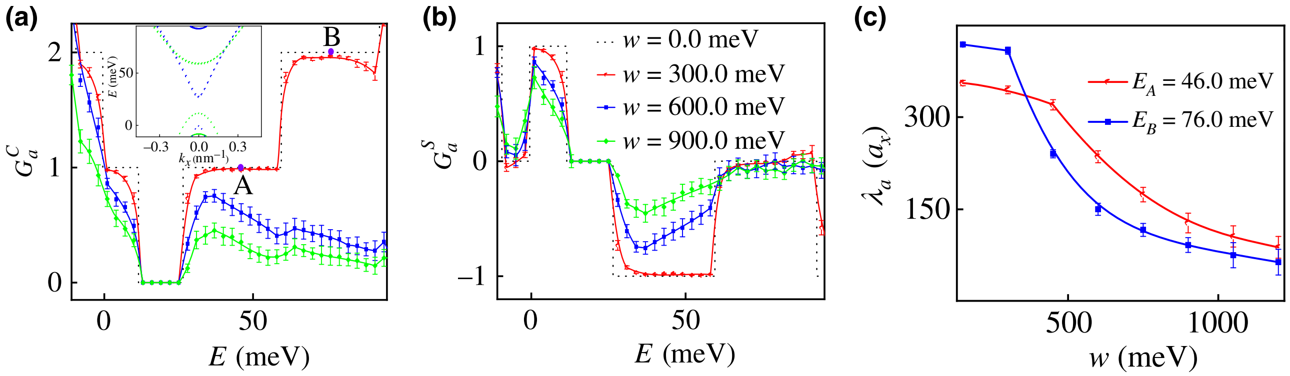

FIG. 5. The ensemble average charge (a) and spin (b) conductance of the disordered system versus the electron energy at different disorder strengths. Inset in (a) shows the corresponding energy band of the TDSM nanowire. (c) The ensemble localization length of the disordered system versus the disorder strength. The gate voltage and magnetic flux are selected at $V_g = 550.0$ mV and $\phi = 4.0 \times 10^{-3}$, respectively. The error bars in (a)–(c) denote the charge-conductance, spin-conductance, and localization-length fluctuations, respectively. The number of the disordered TDSM nanowire samples is chosen as 200.

According to Eqs. (10) and (11), we can find that the bulk subbands of the TDSM film are split. This effect is the physical origin of the Zeeman-like spin-split bulk subbands observed in Fig. 2(c). The lowest bulk LLs ($m = 1, n = 1$) of the TDSM nanofilm as a function of the negative quadratic magnetic length ($\propto B_z$) is shown by the solid lines in Fig. 5(a). The blue lines stand for the spin-down LLs while the green lines for the spin-up ones. It can be seen that the bulk LLs agree qualitatively with those obtained in Fig. 2(c).

Next we consider the influence of the perpendicular MF on the surface states of the TDSM nanowire. For the lowest pair of the surface subbands in Fig. 2(a), its low-energy effective Hamiltonian can be written as [52]

$$H^{\text{SF}} = \hbar v_F \tau_z \sigma_z k_x + \Delta \tau_x, \tag{12}$$

where v_F is the Fermi velocity of the surface states. τ_z and σ_z are the Pauli matrices that stand for the lateral two surfaces and spin, respectively. Δ denotes the opened surface band gap caused by the interaction between these two lateral surface states. When a perpendicular MF is applied, the surface states' Hamiltonian of the TDSM nanowire is

$$H^{\text{SF}} = \begin{bmatrix} \hbar v_F k_+^M & 0 & \Delta & 0 \\ 0 & -\hbar v_F k_+^M & 0 & \Delta \\ \Delta & 0 & -\hbar v_F k_-^M & 0 \\ 0 & \Delta & 0 & \hbar v_F k_-^M \end{bmatrix}, \tag{13}$$

in which $k_\pm^M = k_x \pm k_M$ with the magnetic wave vector $k_M = eB_z W_y / 2\hbar$.

Diagonalizing the Hamiltonian in Eq. (13), the eigenvalues of the surface states are achieved as

$$E_{\pm,s}^{\text{SF}} = s\{(\hbar v_F)^2 (k_x^2 + k_M^2) + \Delta^2 \pm 2\hbar v_F k_M [(\hbar v_F k_x)^2 + \Delta^2]^{1/2}\}^{1/2}, \tag{14}$$

where $s = \pm$ represents two different pairs of the surface subbands. The surface subband edge energies ($k_x = 0$) of the TDSM nanowire as a function of the magnetic wave vector ($\propto B_z$) are depicted by the dotted lines in Fig. 5(b). The blue lines stand for the spin-down subbands while the green lines for the spin-up ones. The Fermi velocity is taken as $v_F = 1.96 \times 10^4$ m/s and the surface gap $\Delta = 46$ meV, which are obtained from the energy band of the pristine TDSM nanowire in Fig. 2(a). It can be found that the surface subbands also agree qualitatively with those obtained in Fig. 2(c). Note that although the Zeeman effect of the MF is not taken into the numerical and analytic calculations above, it can be included simply by adding the Zeeman terms $E_Z = \pm\frac{1}{2} g^* \mu_B B_z$ to the Hamiltonians in Eqs. (1), (5), and (12). Here $+$ and $-$ stand for spin-up and spin-down subbands, respectively. g^* is the effective Landé g factor of TDSM and μ_B is Bohr magneton. For the TDSM Na_3Bi, the Zeeman energy $E_Z = 0.58 B_z$ meV with $g^* = 20$ [30]. Including the Zeeman effect, the lowest pair of bulk LLs and surface-subband-edge energies as a funciton of the MF strength are shown by the dashed lines in Figs. 5(a) and 5(b), respectively. They verify that the Zeeman effect does not change the intrinsic results obtained in this work.

According to the charge- and spin-conductance behaviors in Figs. 3(a) and 3(b), the considered system may be used to design a topological spin filtering and switch device. For the practical application aspect, the robustness of the topological device to impurity scattering should be investigated. The effect of the impurity-induced scattering on the conductances can be simulated by the random fluctuations of the on-site energies of the discrete lattices [43] within the range $[-w/2, w/2]$. Here w means the disorder strength. The ensemble average charge ($G_a^C = \langle G^C \rangle$) and spin ($G_a^S = \langle G^S \rangle$) conductances of disordered TDSM nanowires as a function of the electron energy at different disorder strengths are shown in Figs. 5(a) and 5(b), respectively. Here $\langle \cdots \rangle$ denotes averaging over an ensemble of samples with different realizations of disorder. The number of the disordered TDSM nanowire samples taken for the calculations is 200. The lateral gate voltage is chosen as $V_g = 550.0$ mV and the magnetic flux is set at $\phi = 4.0 \times 10^{-3}$, as indicated by the vertical green and navy dashed lines in Figs. 2(b) and 3(a)–3(b), respectively. The disorder strengths are taken as $w = 300.0$ (red circle lines), 600.0 (blue square lines), and 900.0 (green diamond lines) meV. The error bars in Figs. 5(a) and 5(b) represent the fluctuations of the charge ($G_f^C = [\langle (G^C)^2 \rangle - \langle G^C \rangle^2]^{1/2}$) and spin ($G_f^S = [\langle (G^S)^2 \rangle - \langle G^S \rangle^2]^{1/2}$) conductances [53], respectively. The thin dotted line stands for those of the ideal TDSM nanowire, which is used as a reference. For the weak disorder strength $w = 300.0$ meV, both the surface charge and spin conductances of the TDSM nanowire are still quantized, especially for those conductance amplitudes away from the subband edges, verifying the topological character of the nanowire. As the disorder strength is increased, the quantized charge and spin conductances are destroyed, as shown by the blue square and green diamond lines. However, the amplitudes of the charge and spin conductances within the QAHLI regions are relatively large. More importantly, both the charge and spin conductances still can be switched on or off by varying the electron energy. In order to give a more clear criterion of the conductances against the disorder, the ensemble localization length ($\lambda_a = \langle \lambda \rangle$) of the disordered TDSM nanowire as a function of the disorder strength is shown in Fig. 5(c). The localization length $\lambda = -2/\lim_{L_x \to \infty}(1/L_x) \ln \mathrm{Tr}|G^a G^r|$, where Tr means the trace over the spatial and spin degrees of freedom [54]. The electron energies are taken as $E_A = 46.0$ meV (red circle line) and $E_B = 76.0$ meV (blue square line). These two energies are located at the QAHLI and QSHLI regions, as denoted by points A and B in Fig. 5(a), respectively. Similar to those in Figs. 5(a) and 5(b), the error bar in each line means the localization length fluctuation ($\lambda_f = [\langle \lambda^2 \rangle - \langle \lambda \rangle^2]^{1/2}$). The localized length of the considered system decreases slowly as the the disorder strength is increased. However, as long as the length of the disordered TDSM nonawire is smaller that the localization length, the surface charge and spin conductances will not vanish. These results demonstrate that the proposed topological spin filtering and switch device may be applied in practice.

IV. CONCLUSIONS

In conclusion, the quantum-transport properties of a TDSM nanowire in the presence of two lateral gates and a perpendicular MF are investigated. It is found that both the charge and spin conductances can be controlled by varying the electron energy and MF strength. Therefore, topological spin filtering and switch device is proposed based on the considered system. The work mechanism of the device is attributed to the QAHLI state in the TDSM nanowire caused by the perpendicular MF. Further studies show that the topological spin filtering and switch effect is robust against a strong disorder, indicating that the device has the potential in practical applications.

ACKNOWLEDGMENTS

The authors thank X.Y. Zhou and G.H. Zhou for valuable discussions. This work is supported by the NSFC (Grants No. 11664019, No. 11764013, and No. 11864012), the Science Foundation for Distinguished Young Scholars in Jiangxi Province of China (Grant No. 20162BCB23032), and Jiangxi University of Traditional Chinese Medicine 1050 youth talent project (Grant No. 5142001010).

[1] N. P. Armitage, E. J. Mele, and A. Vishwanath, Weyl and Dirac semimetals in three-dimensional solids, Rev. Mod. Phys. **90**, 015001 (2018).

[2] S. M. Young, S. Zaheer, J. C. Y. Teo, C. L. Kane, E. J. Mele, and A. M. Rappe, Dirac Semimetal in Three Dimensions, Phys. Rev. Lett. **108**, 140405 (2012).

[3] Z. J. Wang, Y. Sun, X. Q. Chen, C. Franchini, G. Xu, H. M. Weng, X. Dai, and Z. Fang, Dirac semimetal and topological phase transitions in A_3Bi (A = Na, K, Rb), Phys. Rev. B **85**, 195320 (2012).

[4] Z. J. Wang, H. M. Weng, Q. S. Wu, X. Dai, and Z. Fang, Three-dimensional Dirac semimetal and quantum transport in Cd_3As_2, Phys. Rev. B **88**, 125427 (2013).

[5] Z. K. Liu, B. Zhou, Y. Zhang, Z. J. Wang, H. M. Weng, D. Prabhakaran, S.-K. Mo, Z. X. Shen, Z. Fang, X. Dai, Z. Hussain, and Y. L. Chen, Discovery of a three-dimensional topological dirac semimetal, Na_3Bi, Science **343**, 864 (2014).

[6] Y. Zhang, Z. K. Liu, B. Zhou, Y.-K. Kim, Z. Hussain, Z. X. Shen, Y. L. Chen, and S.-K. Mo, Molecular beam epitaxial growth of a three-dimensional topological Dirac semimetal Na_3Bi, Appl. Phys. Lett. **105**, 031901 (2014).

[7] J. Wen, H. Guo, C. H. Yan, Z. Y. Wang, K. Chang, P. Deng, T. Zhang, Z. D. Zhang, S. H. Jia, L. L. Wang, K. He, X. C. Ma, X. Chen, and Q. K. Xue, Synthesis of semimetal A_3Bi (A = Na, K) thin films by molecular beam epitaxy, Appl. Surf. Sci. **327**, 213 (2015).

[8] S. Borisenko, Q. Gibson, D. Evtushinsky, V. Zabolotnyy, B. Büchner, and R. J. Cava, Experimental Realization of a Three-Dimensional Dirac Semimetal, Phys. Rev. Lett. **113**, 027603 (2014).

[9] A. Gyenis, H. Inoue, S. Jeon, B. B. Zhou, B. E. Feldman, Z. Wang, J. Li, S. Jiang, Q. D. Gibson, S. K. Kushwaha, J. W. Krizan, N. Ni, R. J. Cava, B. A. Bernevig, and A. Yazdani, Imaging electronic states on topological semimetals using scanning tunneling microscopy, New J. Phys. **18**, 105003 (2016).

[10] M. Neupane, S. Y. Xu, R. Sankar, N. Alidoust, G. Bian, C. Liu, I. Belopolski, T. R. Chang, H. T. Jeng, H. Lin,

A. Bansil, F. C. Chou, and M. Z. Hasan, Observation of a three-dimensional topological Dirac semimetal phase in high-mobility Cd_3As_2, Nat. Commun. **5**, 4786 (2014).

[11] Y. F. Zhao, H. W. Liu, C. L. Zhang, H. C. Wang, J. F. Wang, Z. Q. Lin, Y. Xing, H. Lu, J. Liu, Y. Wang, S. M. Brombosz, Z. L. Xiao, S. Jia, X. C. Xie, and J. Wang, Anisotropic Fermi Surface and Quantum Limit Transport in High Mobility Three-Dimensional Dirac Semimetal Cd_3As_2, Phys. Rev. X **5**, 031037 (2015).

[12] J. Hellerstedt, M. T. Edmonds, N. Ramakrishnan, C. Liu, B. Weber, A. Tadich, K. M. O'Donnell, S. Adam, and M. S. Fuhrer, Electronic properties of high-quality epitaxial topological dirac semimetal thin films, Nano. Lett. **16**, 3210 (2016).

[13] X. Wan, A. M. Turner, A. Vishwanath, and S. Y. Savrasov, Topological semimetal and Fermi-arc surface states in the electronic structure of pyrochlore iridates, Phys. Rev. B **83**, 205101 (2011).

[14] H. M. Yi, Z. J. Wang, C. Y. Chen, Y. G. Shi, Y. Feng, A. J. Liang, Z. J. Xie, S. L. He, J. F. He, Y. Y. Peng, X. Liu, Y. Liu, L. Zhao, G. D. Liu, X. L. Dong, J. Zhang, M. Nakatake, M. Arita, K. Shimada, H. Namatame, M. Taniguchi, Z. Y. Xu, C. T. Chen, X. Dai, Z. Fang, and X. J. Zhou, Evidence of topological surface state in three-dimensional dirac semimetal Cd_3As_2, Sci. Rep. **4**, 6106 (2014).

[15] S. Y. Xu, C. Liu, S. K. Kushwaha, R. Sankar, J. W. Krizan, I. Belopolski, M. Neupane, G. Bian, N. Alidoust, T. R. Chang, H. T. Jeng, C. Y. Huang, W. F. Tsai, H. Lin, P. P. Shibayev, F. C. Chou, R. J. Cava, and M. Z. Hasan, Observation of Fermi arc surface states in a topological metal, Science **347**, 294 (2015).

[16] C. Zhang, J. Sun, F. Liu, A. Narayan, N. Li, X. Yuan, Y. Liu, J. Dai, Y. Long, Y. Uwatoko, J. Shen, S. Sanvito, W. Yang, J. Cheng, and F. Xiu, Evidence for pressure-induced node-pair annihilation in Cd_3As_2, Phys. Rev. B **96**, 155205 (2017).

[17] S. Guan, Z. M. Yu, Y. Liu, G. B. Liu, L. Dong, Y. Lu, Y. Yao, and S. A. Yang, Artificial gravity field, astrophysical analogues, and topological phase transitions in strained topological semimetals, npj Quantum Materials **2**, 23 (2017).

[18] H. Pan, M. Wu, Y. Liu, and S. A. Yang, Electric control of topological phase transitions in Dirac semimetal thin films, Sci. Rep. **5**, 14639 (2015).

[19] J. L. Collins, A. Tadich, W. Wu, L. C. Gomes, J. N. B. Rodrigues, C. Liu, J. Hellerstedt, H. Ryu, S. Tang, S. K. Mo, S. Adam, S. A. Yang, M. S. Fuhrer, and M. T. Edmonds, Electric-field-tuned topological phase transition in ultrathin Na_3Bi, Nature **564**, 390 (2018).

[20] R. Chen, D. H. Xu, and B. Zhou, Topological Anderson insulator phase in a Dirac-semimetal thin film, Phys. Rev. B **95**, 245305 (2017).

[21] S. Jeon, B. B. Zhou, A. Gyenis, B. E. Feldman, I. Kimchi, A. C. Potter, Q. D. Gibson, R. J. Cava, A. Vishwanath, and A. Yazdani, Landau quantization and quasiparticle interference in the three-dimensional Dirac semimetal Cd_3As_2, Nat. Mater. **13**, 851 (2014).

[22] J. Z. Cao, S. H. Liang, C. Zhang, Y. W. Liu, J. W. Huang, Z. Jin, Z. G. Chen, Z. J. Wang, Q. S. Wang, J. Zhao, S. Y. Li, X. Dai, J. Zou, Z. C. Xia, L. Li, and F. X. Xiu, Landau level splitting in Cd_3As_2 under high magnetic fields, Nat. Commun. **6**, 7779 (2015).

[23] Z. J. Xiang, D. Zhao, Z. Jin, C. Shang, L. K. Ma, G. J. Ye, B. Lei, T. Wu, Z. C. Xia, and X. H. Chen, Angular-Dependent Phase Factor of Shubnikov-De Haas Oscillations in the Dirac Semimetal Cd_3As_2, Phys. Rev. Lett. **115**, 226401 (2015).

[24] M. X. Deng, W. Luo, R. Q. Wang, L. Sheng, and D. Y. Xing, Weyl semimetal induced from a Dirac semimetal by magnetic doping, Phys. Rev. B **96**, 155141 (2017).

[25] C. Huang, B. T. Zhou, H. Zhang, B. Yang, R. Liu, H. Wang, Y. Wan, K. Huang, Z. Liao, E. Zhang, S. Liu, Q. Deng, Y. Chen, X. Han, J. Zou, X. Lin, Z. Han, Y. Wang, K. T. Law, and F. Xiu, Proximity-induced surface superconductivity in Dirac semimetal Cd_3As_2, Nat. Commun. **10**, 2217 (2019).

[26] L. P. He, X. C. Hong, J. K. Dong, J. Pan, Z. Zhang, J. Zhang, and S. Y. Li, Quantum Transport Evidence for the Three-Dimensional Dirac Semimetal Phase in Cd_3As_2, Phys. Rev. Lett. **113**, 246402 (2014).

[27] J. Y. Feng, Y. Pang, D. S. Wu, Z. J. Wang, H. M. Weng, J. Q. Li, X. Dai, Z. Fang, Y. G. Shi, and L. Lu, Large linear magnetoresistance in Dirac semimetal Cd_3As_2 with Fermi surfaces close to the Dirac points, Phys. Rev. B **92**, 081306(R) (2015).

[28] A. Narayanan, M. D. Watson, S. F. Blake, N. Bruyant, L. Drigo, Y. L. Chen, D. Prabhakaran, B. Yan, C. Felser, T. Kong, P. C. Canfield, and A. I. Coldea, Linear Magnetoresistance Caused by Mobility Fluctuations in n-Doped Cd_3As_2, Phys. Rev. Lett. **114**, 117201 (2015).

[29] C. Z. Li, L. X. Wang, H. W. Liu, J. Wang, Z. M. Liao, and D. P. Yu, Giant negative magnetoresistance induced by the chiral anomaly in individual Cd_3As_2 nanowires, Nat. Commun. **6**, 10137 (2015).

[30] J. Xiong, S. K. Kushwaha, T. Liang, J. W. Krizan, M. Hirschberger, W. Wang, R. J. Cava, and N. P. Ong, Evidence for the chiral anomaly in the Dirac semimetal Na_3Bi, Science **350**, 413 (2015).

[31] H. Li, H. T. He, H. Z. Lu, H. C Zhang, H. C. Liu, R. Ma, Z. Y. Fan, S. Q. Shen, and J. N. Wang, Negative magnetoresistance in Dirac semimetal Cd_3As_2, Nat. Commun. **7**, 10301 (2016).

[32] G. Zheng, J. Lu, X. Zhu, W. Ning, Y. Han, H. Zhang, J. Zhang, C. Xi, J. Yang, H. Du, K. Yang, Y. Zhang, and M. Tian, Transport evidence for the three-dimensional Dirac semimetal phase in $ZrTe_5$, Phys. Rev. B **93**, 115414 (2016).

[33] B. Zhao, P. Cheng, H. Pan, S. Zhang, B. Wang, G. Wang, F. Xiu, and F. Song, Weak antilocalization in Cd_3As_2 thin films, Sci. Rep. **6**, 22377 (2016).

[34] Y. Wang, E. Liu, H. Liu, Y. Pan, L. Zhang, J. Zeng, Y. Fu, M. Wang, K. Xu, Z. Huang, Z. Wang, H. Z. Lu, D. Xing, B. Wang, X. Wan, and F. Miao, Gate-tunable negative longitudinal magnetoresistance in the predicted type-II Weyl semimetal WTe_2, Nat. Commun. **7**, 13142 (2016).

[35] Z. B. Siu, Mansoor B. A. Jalil, and S. G. Tan, Dirac semimetal thin films in in-plane magnetic fields, Sci. Rep. **6**, 34882 (2016).

[36] X. S. Li, C. Wang, M. X. Deng, H. J. Duan, P. H. Fu, R. Q. Wang, L. Sheng, and D. Y. Xing, Photon-Induced

Weyl Half-Metal Phase and Spin Filter Effect from Topological Dirac Semimetals, Phys. Rev. Lett. **123**, 206601 (2019).

[37] Y. Liu, X. Yuan, C. Zhang, Z. Jin, A. Narayan, C. Luo, Z. Chen, L. Yang, J. Zou, X. Wu, S. Sanvito, Z. Xia, L. Li, Z. Wang, and F. Xiu, Zeeman splitting and dynamical mass generation in Dirac semimetal $ZrTe_5$, Nat. Commun. **7**, 12516 (2016).

[38] C. Zhang, Y. Zhang, X. Yuan, S. Lu, J. Zhang, A. Narayan, Y. Liu, H. Zhang, Z. Ni, R Liu, E. S. Choi, A. Suslov, S. Sanvito, L. Pi, H. Z. Lu, A. C. Potter, and F. Xiu, Quantum Hall effect based on Weyl orbits in Cd_3As_2, Nature **565**, 331 (2019).

[39] F. Tang, Y. Ren, P. Wang, R. Zhong, J. Schneeloch, S. A. Yang, K. Yang, P. A. Lee, G. Gu, Z. Qiao, and L. Zhang, Three-dimensional quantum Hall effect and metal-insulator transition in $ZrTe_5$, Nature **569**, 537 (2019).

[40] C. M. Wang, H. P. Sun, H. Z. Lu, and X. C. Xie, 3D Quantum Hall Effect of Fermi Arcs in Topological Semimetals, Phys. Rev. Lett. **119**, 136806 (2017).

[41] S. Wang, B. C. Lin, W. Z. Zheng, D. Yu, and Z. M. Liao, Fano Interference between Bulk and Surface States of a Dirac Semimetal Cd_3As_2 Nanowire, Phys. Rev. Lett. **120**, 257701 (2018).

[42] B. C. Lin, S. Wang, A. Q. Wang, Y. Li, R. R. Li, K. Xia, D. Yu, and Z. M. Liao, Electric Control of Fermi Arc Spin Transport in Individual Topological Semimetal Nanowires, Phys. Rev. Lett. **124**, 1168021 (2020).

[43] X. B. Xiao, S. A. Yang, Z. F. Liu, H. L. Li, and G. H. Zhou, Anisotropic quantum confinement effect and electric control of surface states in dirac semimetal nanostructures, Sci. Rep. **5**, 7898 (2015).

[44] X. Xiao, Z. Liu, Q. Wu, Y. Li, F. Li, and Y. Du, Anisotropic magnetoelectronic structures and magneto-transport properties of topological Dirac semimetal nanowires, J. Magn. Magn. Mater. **484**, 373 (2019).

[45] T. Ando, Quantum point contacts in magnetic fields, Phys. Rev. B **44**, 8017 (1991).

[46] X. B. Xiao, H. L. Li, G. H. Zhou, and N. H. Liu, Spin-dependent electron transport in a Rashba quantum wire with rough edges, Eur. Phys. J. B **85**, 305 (2012).

[47] M. Büttiker, Four-Terminal Phase-Coherent Conductance, Phys. Rev. Lett. **57**, 1761 (1986).

[48] T. P. Pareek and P. Bruno, Magnetic scanning tunneling microscopy with a two-terminal nonmagnetic tip: Quantitative results, Phys. Rev. B **63**, 165424 (2001).

[49] K. B. Nikolić and S. Souma, Decoherence of transported spin in multichannel spin-orbit-coupled spintronic devices: Scattering approach to spin-density matrix from the ballistic to the localized regime, Phys. Rev. B **71**, 195328 (2005).

[50] J. Hellerstedt, I. Yudhistira, M. T. Edmonds, C. Liu, J. Collins, S. Adam, and M. S. Fuhrer, Electrostatic modulation of the electronic properties of Dirac semimetal Na_3Bi thin films, Phys. Rev. Mater. **1**, 054203 (2017).

[51] B. Zhou, H. Z. Lu, R. L. Chu, S. Q. Shen, and Q. Niu, Finite Size Effects on Helical Edge States in a Quantum Spin-Hall System, Phys. Rev. Lett. **101**, 246807 (2008).

[52] C. L. Kane and E. J. Mele, Quantum Spin Hall Effect in Graphene, Phys. Rev. Lett. **95**, 226801 (2005); Z_2 Topological Order and the Quantum Spin Hall Effect, *ibid.* **95**, 146802 (2006); B. A. Bernevig, T. L. Hughes, and S. C. Zhang, Quantum spin Hall effect and topological phase transition in HgTe quantum wells, Science **314**, 1757 (2006); M. Buttiker, Physics. Edge-state physics without magnetic fields, *ibid.* **325**, 278 (2009); M. Z. Hasan and C. L. Kane, Colloquium: Topological insulators, Rev. Mod. Phys. **82**, 3045 (2010); X.-L. Qi and S.-C. Zhang, Topological insulators and superconductors, *ibid.* **83**, 1057 (2011).

[53] K. Nikolić and A. MacKinnon, Conductance and conductance fluctuations of narrow disordered quantum wires, Phys. Rev. B **50**, 11008 (1994).

[54] K. Nikolić and A. MacKinnon, Density of states and localization length in compositionally disordered quantum wires, Phys. Rev. B **47**, 6555 (1993).